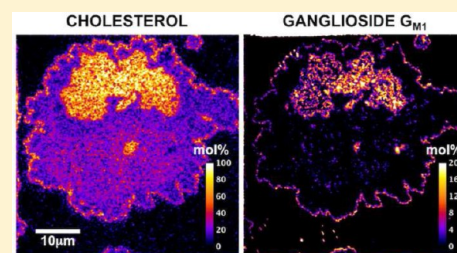


Colocalization of the Ganglioside  $G_{M1}$  and Cholesterol Detected by Secondary Ion Mass SpectrometryMónica M. Lozano,<sup>\*,†</sup> Zhao Liu,<sup>§</sup> Eva Sunnick,<sup>‡</sup> Andreas Janshoff,<sup>‡</sup> Krishna Kumar,<sup>\*,§,||</sup> and Steven G. Boxer<sup>\*,†</sup><sup>†</sup>Department of Chemistry, Stanford University, Stanford, California 94305-5080, United States<sup>‡</sup>Institute of Physical Chemistry, University of Göttingen, Tammannstrasse 6, 37077 Göttingen, Germany<sup>§</sup>Department of Chemistry, Tufts University, Medford, Massachusetts 02155-5813, United States<sup>||</sup>Cancer Center, Tufts Medical Center, Boston, Massachusetts 02110, United States

## S Supporting Information

**ABSTRACT:** The characterization of the lateral organization of components in biological membranes and the evolution of this arrangement in response to external triggers remain a major challenge. The concept of lipid rafts is widely invoked; however, direct evidence of the existence of these ephemeral entities remains elusive. We report here the use of secondary ion mass spectrometry (SIMS) to image the cholesterol-dependent cohesive phase separation of the ganglioside  $G_{M1}$  into nano- and microscale assemblies in a canonical lipid raft composition of lipids. This assembly of domains was interrogated in a model membrane system composed of palmitoyl sphingomyelin (PSM), cholesterol, and an unsaturated lipid (dioleoylphosphatidylcholine, DOPC). Orthogonal isotopic labeling of every lipid bilayer component and monofluorination of  $G_{M1}$  allowed generation of molecule specific images using a NanoSIMS. Simultaneous detection of six different ion species in SIMS, including secondary electrons, was used to generate ion ratio images whose signal intensity values could be correlated to composition through the use of calibration curves from standard samples. Images of this system provide the first direct, molecule specific, visual evidence for the colocalization of cholesterol and  $G_{M1}$  in supported lipid bilayers and further indicate the presence of three compositionally distinct phases: (1) the interdomain region; (2) micrometer-scale domains ( $d > 3 \mu\text{m}$ ); (3) nanometer-scale domains ( $d = 100 \text{ nm}$  to  $1 \mu\text{m}$ ) localized within the micrometer-scale domains and the interdomain region. PSM-rich, nanometer-scale domains prefer to partition within the more ordered, cholesterol-rich/DOPC-poor/ $G_{M1}$ -rich micrometer-scale phase, while  $G_{M1}$ -rich, nanometer-scale domains prefer to partition within the surrounding, disordered, cholesterol-poor/PSM-rich/DOPC-rich interdomain phase.



## ■ INTRODUCTION

It is generally believed that certain membrane lipids and membrane-anchored proteins tend to associate in the plasma membrane and that this clustering is important for function; however, it has proven to be difficult to characterize this association because of both the small size of the assemblies and their transient nature. In particular, the concept of lipid rafts<sup>1</sup> posits that 10–100 nm assemblies enriched in sphingolipids, glycosphingolipids, such as the ganglioside  $G_{M1}$ , cholesterol, and glycosphosphatidylinositol (GPI) anchored proteins<sup>2</sup> are important for membrane function. One limitation of many experimental approaches to this problem is the inherent perturbation on the lateral organization by labels that serve to provide feedback in the form of luminescence or paramagnetic signals. Introduction of labels can change the behavior of endogenous lipids leading to ambiguity and can be a major source of irreconcilable data among different laboratories using different probes. An extensive literature has evolved on the phase behavior of multicomponent lipid mixtures,<sup>3</sup> and while this may not be directly relevant to cellular membranes, it provides a benchmark for understanding

complex biological systems. However, even these studies typically involve partitioning of dyes or other labels among different phases and do not directly measure the composition of the phases. For this reason, imaging mass spectrometry, directly measuring the mass of components or isotopically labeled fragments from the components, offers an attractive alternative approach.

Optical methods have been extensively used to obtain information on lipid rafts, including indirect imaging approaches such as single particle and fluorophore tracking,<sup>4–6</sup> Förster resonance energy transfer (FRET),<sup>7,8</sup> homo-FRET,<sup>9</sup> fluorescence correlation and cross-correlation spectroscopy,<sup>10</sup> and super-resolution techniques.<sup>11–20</sup> These techniques use fluorescently labeled membrane components making direct comparisons between the labeled analogues and the native molecules difficult, especially in the case of the lipid components. For instance, many of the best fluorescent dyes are as large as the lipids they label and often have charges or

Received: November 8, 2012

Published: March 20, 2013

large hydrophobic regions that may interact with the membrane. Nonetheless, experimental observations point to the existence of nanometer scale assemblies in the plasma membrane. In particular, a stimulated emission depletion (STED) microscopy study revealed that a cholesterol-dependent phase hindered the diffusion of Atto647N-labeled sphingomyelin, ganglioside  $G_{M1}$ , and a GPI-anchored protein within <20 nm diameter areas in the plasma membrane.<sup>17</sup> Spin label measurements have also proven to be useful,<sup>8,21</sup> as have more direct imaging techniques such as amplitude<sup>22</sup> and frequency<sup>23–27</sup> modulation atomic force microscopy (AFM) and electron microscopy.<sup>28</sup>

Imaging mass spectrometry offers an alternative approach. The most important advantages are that these methods are free of added labels, and direct information is obtained on the composition of membrane components that can be made quantitative in some cases. We note that such measurements are made in high vacuum; thus, a great deal of effort is required to faithfully capture and preserve the sample and only snapshots of dynamic processes can be obtained. Time-of-flight secondary ion mass spectrometry (ToF-SIMS)<sup>29–32</sup> and matrix-assisted laser desorption/ionization (MALDI) and MALDI-ToF<sup>33,34</sup> have been used to image the lateral organization and composition of biological tissue sections<sup>32,34</sup> as well as model and cell membranes.<sup>29,30,33</sup> ToF-SIMS has the advantage of high information content, as large molecular fragments are detected and very high spatial resolution is possible; however, ionization efficiencies for different components vary substantially making quantification difficult, and the sensitivity of the current instruments is modest. We have advocated the use of multiple-isotope mass spectrometry<sup>35</sup> (MIMS) using a NanoSIMS (Cameca Instruments) as an imaging tool for interrogating membrane composition.<sup>36–39</sup> This technique requires isotopic labeling or atom exchange (e.g., with F) of membrane components but can generate molecule-specific images with high spatial resolution, high sensitivity, and high mass resolving power, and calibration samples can be used to obtain quantitative estimates of the composition of each component. The NanoSIMS uses a continuous primary ion beam of either cesium (for generating negative secondary ions) or oxygen (for generating positive secondary ions). A spatial resolution of 50 nm or better is achieved by a coaxial optical configuration where primary and secondary ion beams are colocalized perpendicularly to the sample. Image acquisition is achieved by rastering the primary ion beam across a region of interest as illustrated in Figure 1. Secondary negative ions, including atomic ions such as  $^{12}\text{C}^-$  and/or  $^{13}\text{C}^-$ ,  $^{19}\text{F}^-$  (added as a label),  $^{31}\text{P}^-$ , and  $^{32}\text{S}^-$  or molecular ions such as  $\text{CN}^-$  ( $^{12}\text{C}^{14}\text{N}^-$ ,  $^{12}\text{C}^{15}\text{N}^-$ ,  $^{13}\text{C}^{14}\text{N}^-$ , and  $^{13}\text{C}^{15}\text{N}^-$ ),  $\text{CH}^-$  ( $^{12}\text{C}^1\text{H}^-$ ,  $^{13}\text{C}^1\text{H}^-$ ,  $^{12}\text{C}^2\text{H}^-$ , and  $^{13}\text{C}^2\text{H}^-$ ) and others, are ejected from the sample and focused through a lens forming a secondary ion beam that is accelerated into a magnetic sector and channeled into a set of detectors (seven on the NanoSIMS 50L) according to their mass-to-charge ratio. Consequently, secondary ion intensities are collected from exactly the same volume of material to obtain molecule-specific images. In contrast to most methods, the location and composition of all components can be visualized, including the correlated colocalization of components.

In this study, secondary ion mass spectrometry was used to image the cholesterol-dependent cohesive phase separation of the ganglioside  $G_{M1}$  into nanometer and micrometer scale assemblies within the widely used phase separated model

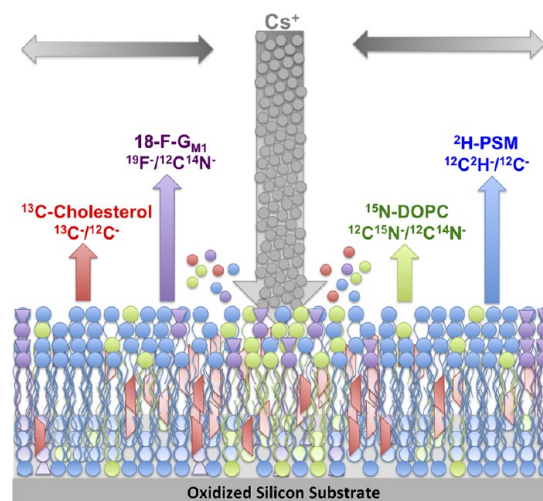
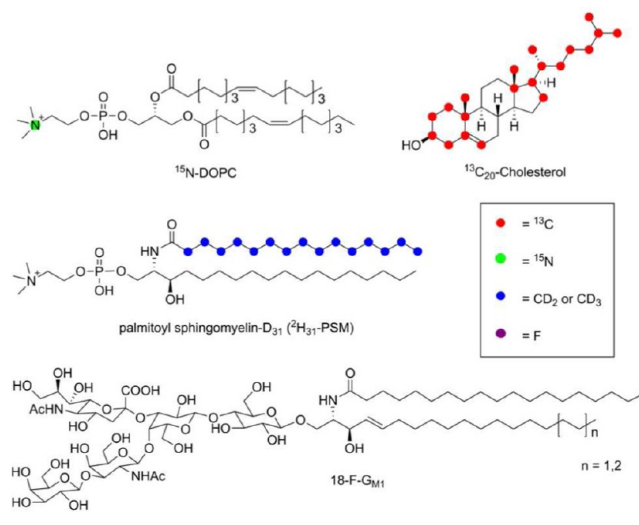


**Figure 1.** Schematic of the NanoSIMS experiments. A cesium ion beam is rastered across a surface generating secondary ions ( $^{12}\text{C}^-$ ,  $^{13}\text{C}^-$ ,  $^{12}\text{C}^2\text{H}^-$ ,  $^{19}\text{F}^-$ ,  $^{12}\text{C}^{14}\text{N}^-$ , and  $^{12}\text{C}^{15}\text{N}^-$ ) from the components of a supported lipid bilayer shown as a phase separated mixture of  $^{13}\text{C}$ -cholesterol,  $^2\text{H}_{31}$ -palmitoyl sphingomyelin ( $^2\text{H}$ -PSM),  $^{18}\text{F}$ - $G_{M1}$ , and  $^{15}\text{N}$ -DOPC (see Scheme 1).

#### Scheme 1. Structural Representatives of Labeled Molecules To Facilitate NanoSIMS Analysis of Supported Lipid Bilayers



membrane system composed of palmitoyl sphingomyelin (PSM), cholesterol, and an unsaturated lipid. These measurements are possible because  $G_{M1}$ , with a single F atom at position 18 of the stearic acid chain (Scheme 1), provides a sensitive probe of its location without affecting biological functionality. As illustrated in Figure 1, the lipid bilayer whose lateral composition we wish to profile is supported on an  $\text{SiO}_2/\text{Si}$  substrate. The case illustrated here is a canonical lipid raft mixture consisting of cholesterol (labeled with  $^{13}\text{C}$  and directly detected as  $^{13}\text{C}^-$ ; see Scheme 1), PSM (with one of the two palmitic acid chains fully labeled with  $^2\text{H}$  and detected as  $^{12}\text{C}^2\text{H}^-$ ), ganglioside  $G_{M1}$  (monofluorinated =  $^{18}\text{F}$ - $G_{M1}$ , by replacing an H atom on the terminal methyl group of the stearic acid chain with an F atom<sup>40</sup> and detected as  $^{19}\text{F}^-$ ), and dioleoylphosphatidylcholine (DOPC,  $^{15}\text{N}$ -labeled<sup>38</sup> and detected as  $^{12}\text{C}^{15}\text{N}^-$ ; see Materials and Methods for labeling

details). Ratio ion images were obtained by normalizing the  $^{13}\text{C}^-$  and  $^{12}\text{C}^2\text{H}^-$  ion signals with the  $^{12}\text{C}^-$  ion signal and the  $^{19}\text{F}^-$  and  $^{12}\text{C}^{15}\text{N}^-$  ion signals with the  $^{12}\text{C}^{14}\text{N}^-$  ion signal to minimize systematic signal intensity variations that arose during the measurements. The imaging results are consistent with the formation of submicrometer domains in which cholesterol, PSM, and  $\text{G}_{\text{M1}}$  are enriched.

## MATERIALS AND METHODS

**Biosynthesis of  $^{13}\text{C}$ -Labeled Cholesterol.** Highly  $^{13}\text{C}$  enriched cholesterol is not available commercially, so an efficient system was developed to produce it for these experiments. A major effort is required to produce isotopically labeled cell membrane components in order to unambiguously identify the molecules in a lipid bilayer sample imaged by a NanoSIMS. Isotopically labeled phospholipids (i.e.,  $^{13}\text{C}$ -DSPC and  $^{15}\text{N}$ -DLPC) can be synthesized by adapting conventional methods.<sup>38</sup> However, cholesterol is much more difficult to obtain, and a substantial effort was devoted to the preparation of  $^{13}\text{C}$ -labeled cholesterol. Since only mammalian cells produce cholesterol naturally, although a *Saccharomyces cerevisiae* strain has been engineered to produce cholesterol,<sup>41</sup> human cells known to synthesize high levels of cholesterol were used. Hep G2 cells, derived from a human hepatoblastoma, are adherent cells known to synthesize triglycerides and cholesterol with many similarities to normal liver. Cholesterol biosynthesis in the presence of  $^{13}\text{C}$ -labeled cholesterol precursors (i.e., acetate, acetoacetate, mevalonate, or octanoate) produces a discrete spectrum of cholesterol isotopomers whose enrichment is dictated by growth conditions.<sup>42</sup> Once synthesized, total lipid extraction, separation, and purification steps are performed to isolate the  $^{13}\text{C}$ -cholesterol isotopomers (see Supporting Information for details). Cholesterol isolated from Hep G2 cells grown in acetate with both methyl and carboxyl carbons substituted with  $^{13}\text{C}$  (99%) had an isotopomer distribution ranging from zero to 27  $^{13}\text{C}$  atoms per cholesterol with a concomitant  $^{13}\text{C}/^{12}\text{C}$  ratio of  $\sim 3.07$  corresponding to an average of 20  $^{13}\text{C}$  atoms per cholesterol (Scheme 1 and Figure S1 in Supporting Information).<sup>43</sup>

**Synthesis of  $^{15}\text{N}$ -DOPC.**  $^{15}\text{N}$ -DOPC was synthesized by furnishing DOPG with  $^{15}\text{N}$ -choline as previously described (Scheme 1).<sup>39</sup> (See Supporting Information for details.)

**Synthesis of Monofluorinated  $\text{G}_{\text{M1}}$ .** Monofluorinated  $\text{G}_{\text{M1}}$  (18-F- $\text{G}_{\text{M1}}$ , Scheme 1) was synthesized by coupling lyso- $\text{G}_{\text{M1}}$  with the corresponding fluorinated stearic acid. Lyso- $\text{G}_{\text{M1}}$  was obtained by alkaline hydrolysis of native  $\text{G}_{\text{M1}}$ <sup>44</sup> and then treated with the *N*-hydroxysuccinimide (NHS) ester of the monofluorinated stearic acid to afford fluorinated  $\text{G}_{\text{M1}}$ .<sup>40</sup> The effect of fluorination of  $\text{G}_{\text{M1}}$  on its biological functions in cell membranes as well as its phase behavior properties in model membranes was interrogated by calcium signaling assays, FACS analysis, and AFM imaging of supported lipid bilayers (SLBs). (See details and Figures S2–S4 in Supporting Information.)

**Sample Preparation for NanoSIMS.** *Materials.* Silicon wafers (4 in. (100) p-type) were from Silicon Quest International. Platinum wires ( $d = 1$  mm) and Texas Red 1,2-dihexadecanoyl-*sn*-glycero-3-phosphoethanolamine (TR-DHPE) were from Sigma-Aldrich.  $^2\text{H}_{31}$ -Palmitoyl sphingomyelin ( $^2\text{H}$ -PSM) was from Avanti Polar Lipids Inc.

*Substrates.* Sample preparation is mainly dictated by the requirements of NanoSIMS analysis. Supported lipid bilayers were formed on patterned substrates.<sup>38,39</sup> The patterning grid provides a map of the surface, since the sample needs to be characterized with multiple methods requiring that the same regions be found on separate instruments (typically imaging ellipsometry, fluorescence and atomic force microscopies). Chrome-patterned oxidized silicon supports were prepared with standard methods at the Stanford Nanofabrication Laboratory. Briefly, silicon wafers are thoroughly cleaned to remove trace organics and metals and the natural oxide layer is etched away. A Tylan oxidation furnace is used to thermally grow a thin silicon oxide (silica) film ( $\sim 10$  nm) on the silicon wafer surface. The choice of silicon oxide thickness is an optimal balance between stable lipid bilayer formation and maximal surface charge dissipation for

NanoSIMS.<sup>36</sup> A grid (25, 50, or 100  $\mu\text{m}$ ) pattern composed of chrome (5 nm in height, 5  $\mu\text{m}$  in width) is imprinted using standard photolithography techniques. The wafers are then diced into 5 mm  $\times$  5 mm chips that fit into the NanoSIMS sample holder.

**Preparation of Supported Lipid Bilayers.** Supported lipid bilayers were formed by fusion of giant unilamellar vesicles (GUVs) onto  $\text{SiO}_2/\text{Si}$  substrates. GUVs were used rather than SUVs because their formation consumes substantially less isotopically labeled lipids than SUVs produced by extrusion. Furthermore, deposition and annealing of GUVs to oxidized silicon substrates are less complex than those of SUVs, allowing a much wider range of compositions to be tested. As a result, supported lipid bilayer islands, typically tens of square micrometers in average area, are deposited rather than a continuous supported lipid bilayer. As described below, this has the consequence that the supported bilayers have edges and the composition near the edge of a lipid bilayer can be atypical and is generally ignored. Briefly, lipid bilayer mixtures were prepared by mixing lipids and cholesterol dissolved in chloroform at a 2:2:1  $^2\text{H}$ -PSM/ $^{15}\text{N}$ -DOPC/ $^{13}\text{C}$ -cholesterol ratio with 5 mol % 18-F- $\text{G}_{\text{M1}}$  followed by the complete evaporation of chloroform using a gentle stream of  $\text{N}_2$  while vortexing and allowed to incubate for 1 h in a vacuum desiccator. The lipid mixture was redissolved in  $\text{CHCl}_3$  at a total lipid concentration of 5 mM. GUVs were made via electrosweating<sup>45</sup> by spreading 10  $\mu\text{L}$  of the lipid mixture using a Hamilton syringe to make an even coating over two platinum electrodes of a custom-made electroformation chamber followed by evaporation of  $\text{CHCl}_3$  with a gentle stream of  $\text{N}_2$  and 2 h of incubation in a vacuum desiccator. The chamber was then sealed using vacuum grease with two siliconized glass slides, filled with 200 mM degassed sucrose in water (Milli-Q  $\text{H}_2\text{O}$ , resistivity of  $\sim 18$   $\text{M}\Omega\cdot\text{cm}$ ), and placed on a heating plate at 85  $^\circ\text{C}$ . The electrodes were then connected to a function generator producing a sine wave (amplitude of 3 V, frequency of 10 Hz) for 2 h. The GUV solution was then transferred into an Eppendorf tube and placed in a water bath at 85  $^\circ\text{C}$  for 40 min. The GUV solution was then mixed with an equal volume of preheated 0.73 $\times$  PBS (85  $^\circ\text{C}$ ), and 125  $\mu\text{L}$  of this mixture was added over each  $\text{SiO}_2/\text{Si}$  substrate and incubated for 1 h to allow the formation of lipid bilayer islands by GUV fusion into the substrate. The samples were then rinsed with 3  $\times$  1 mL of degassed  $\text{H}_2\text{O}$  (Milli-Q, resistivity of  $\sim 18$   $\text{M}\Omega\cdot\text{cm}$ ) to remove excess GUVs. The lipid bilayer islands were thermally treated/annealed to allow the formation of separate phases that are closer to equilibrium by placing the samples in an oven at 70  $^\circ\text{C}$  for 30 min and cooled slowly to room temperature at a cooling rate of 5  $^\circ\text{C}/\text{h}$  for a total of  $\sim 9$  h.

Because NanoSIMS analysis takes place in ultra high vacuum, lipid bilayer samples must be dehydrated. To preserve the lateral organization of lipid bilayers formed in an aqueous environment, techniques from freeze-fracture and cryo-EM were applied. Briefly, supported lipid bilayer samples on the NanoSIMS supports were carefully removed from their aqueous environment with tweezers, flicked once to remove excess surface water, and flash-frozen by plunging quickly into liquid ethane at liquid nitrogen temperature ( $-196$   $^\circ\text{C}$ ). Samples were then transferred to a chamber bathed in liquid  $\text{N}_2$  and then subjected to reduced pressures (40–50  $\mu\text{bar}$ ) generated by an oil-free scroll pump equipped with a liquid  $\text{N}_2$  trap for at least 12 h to remove any vitreous ice. The final product was a dehydrated lipid bilayer shown to have identical features from its original hydrated state.<sup>38</sup>

To ensure the level of quality required for NanoSIMS analysis, samples were first visualized by fluorescence microscopy (see Figure S5 in Supporting Information) to establish the overall quality of the freeze-drying process and locate the membrane patches for NanoSIMS imaging. Fluorescence is not used here to establish the phase behavior of the lipid bilayer. A low concentration of a fluorescently labeled lipid (i.e., 0.05 mol % TR-DHPE) added to the lipid mixture allows for the visualization of supported lipid bilayers by a Nikon Eclipse 80i epifluorescence microscope equipped with an Andor Clara camera.

**Secondary Ion Mass Spectrometry.** SIMS imaging was performed using the NanoSIMS 50L instrument at Stanford University, CA. The measurements were made in “images” analysis selection mode using a  $\sim 2$  pA  $^{133}\text{Cs}^+$  primary ion beam (with an



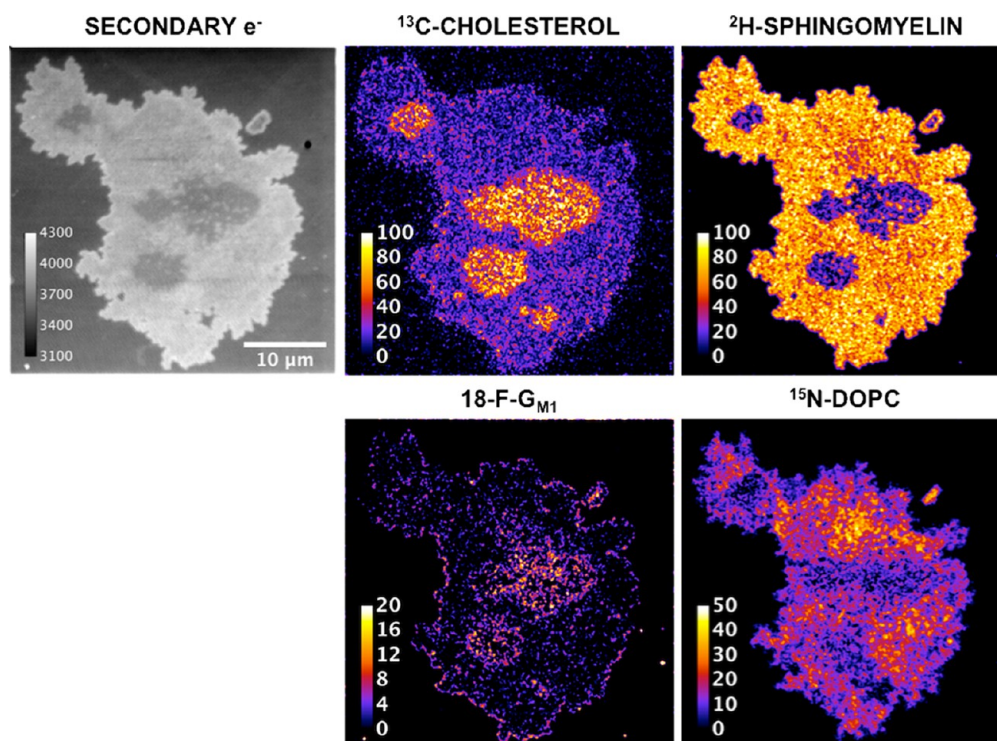


**Figure 2.** NanoSIMS images of a freeze-dried supported lipid bilayer formed by the fusion of a giant unilamellar vesicle composed of 2:2:1  $^2\text{H}$ -sphingomyelin/ $^{15}\text{N}$ -DOPC/ $^{13}\text{C}$ -cholesterol with 5 mol % 18-F- $\text{G}_{\text{M1}}$  to an  $\text{SiO}_2/\text{Si}$  substrate highlighting each component by isotopic or fluorine label along with a secondary electron image. Gray scale bar in secondary electron image represents secondary electron counts. Color bars in molecule-specific images represent percent molar composition from quantitative analysis.

approximate 8% conversion based on the detection  $^{28}\text{Si}^-$  secondary ions from a Si wafer) focused to a  $\sim 100$  nm diameter spot and rastered over sample areas that were  $20\ \mu\text{m} \times 20\ \mu\text{m}$  to  $50\ \mu\text{m} \times 50\ \mu\text{m}$ . The images consisted of 10 replicate scans (i.e., it requires at most 10 frames to burrow through the entire lipid bilayer based on the depletion of molecule-specific secondary ions, including  $^{13}\text{C}^-$ ,  $^{12}\text{C}^2\text{H}^-$ ,  $^{19}\text{F}^-$ , and  $^{12}\text{C}^{15}\text{N}^-$ ) of  $512 \times 512$  pixels with a dwell time of 1 ms/pixel. Secondary ion intensities for  $^{12}\text{C}^-$ ,  $^{13}\text{C}^-$ ,  $^{12}\text{C}^2\text{H}^-$ ,  $^{19}\text{F}^-$ ,  $^{12}\text{C}^{14}\text{N}^-$ , and  $^{12}\text{C}^{15}\text{N}^-$  were collected simultaneously in multicollection mode. Mass resolving powers of  $\sim 8900$  and  $\sim 5600$  were used to separate isobaric interferences:  $^{12}\text{C}^2\text{H}^-$  from  $^{13}\text{C}^1\text{H}^-$  and  $^{12}\text{C}^1\text{H}_2^-$  at mass 14 and  $^{12}\text{C}^{15}\text{N}^-$  from  $^{13}\text{C}^{14}\text{N}^-$  at mass 27, respectively (see Figure S6 in Supporting Information). Samples were also simultaneously imaged using secondary electrons.

**Image Analysis.** Data analysis was performed using the open source software Open MIMS, which is an Image J (version 1.44o, National Institutes of Health, U.S.) plugin. The NanoSIMS secondary ion intensities for  $^{13}\text{C}^-$  and  $^{12}\text{C}^2\text{H}^-$  were normalized to  $^{12}\text{C}^-$  while  $^{19}\text{F}^-$  and  $^{12}\text{C}^{15}\text{N}^-$  were normalized to  $^{12}\text{C}^{14}\text{N}^-$  to minimize systematic signal intensity variations that arose during the measurements. For qualitative (i.e., visualization) purposes only, each ratio image was smoothed (binned) by replacing the pixel value with the average of its  $3 \times 3$  neighboring pixels for noise reduction while the original image was used for all quantitative analyses.

**Standard Samples for Calibration of Lipid and Cholesterol Content.** For each isotopically labeled lipid bilayer component, standard samples that systematically varied in isotopic enrichment were employed for calibration. The concentration of the isotopically labeled component (i.e., 0, 20, 40, 60, 80, 100 mol %) was varied through the addition of the corresponding unlabeled component (i.e., cholesterol added to  $^{13}\text{C}$ -cholesterol, PSM added to  $^2\text{H}$ -PSM,  $\text{G}_{\text{M1}}$  added to 18-F- $\text{G}_{\text{M1}}$ , and DOPC added to  $^{15}\text{N}$ -DOPC) while keeping the total lipid/cholesterol content the same. For each component, the desired mixtures were dissolved in chloroform and spread over  $\text{SiO}_2/\text{Si}$  substrates. Ion intensity ratios (i.e.,  $^{13}\text{C}^-/^{12}\text{C}^-$ ,  $^{12}\text{C}^2\text{H}^-/^{12}\text{C}^-$ ,  $^{19}\text{F}^-/^{12}\text{C}^{14}\text{N}^-$ , and  $^{12}\text{C}^{15}\text{N}^-/^{12}\text{C}^{14}\text{N}^-$ ) were calculated for each

mixture by counting, in “isotopes” analysis selection mode, all  $^{12}\text{C}^-$ ,  $^{13}\text{C}^-$ ,  $^{12}\text{C}^2\text{H}^-$ ,  $^{19}\text{F}^-$ ,  $^{12}\text{C}^{14}\text{N}^-$ , and  $^{12}\text{C}^{15}\text{N}^-$  secondary ions generated using a  $\sim 2$  pA  $^{133}\text{Cs}^+$  primary ion beam scanned 12 times over a  $20\ \mu\text{m} \times 20\ \mu\text{m}$  area ( $256 \times 256$  pixels) with a beam dwell time of 1 ms/pixel. At least three separate ion intensity ratios per standard sample were obtained and plotted against the molar percent composition of the labeled component, and the best-fit line with regression bands were determined (see Figure S7 and Tables S1 and S2 in Supporting Information).

**Quantitative Analysis of Lipid Content.** A two-step calculation was used to estimate the percent molar concentration of each component within regions of interest. First, the calibration curves described above were used to correlate the ratio of intensity values ( $^{13}\text{C}^-/^{12}\text{C}^-$ ,  $^{12}\text{C}^2\text{H}^-/^{12}\text{C}^-$ ,  $^{19}\text{F}^-/^{12}\text{C}^{14}\text{N}^-$ , and  $^{12}\text{C}^{15}\text{N}^-/^{12}\text{C}^{14}\text{N}^-$ ) collected from a specific region of the bilayers to the percent molar composition of the labeled component. Second, the composition within a region of interest was normalized such that the total lipid content was 100 mol %. The uncertainty in the percent molar composition was estimated from the uncertainty in the ratio (from Poisson counting statistics) and the uncertainty in the best fit-line of the calibration curve (from regression bands, see Figures S8–S12 and Table S3–S5 in Supporting Information).

## RESULTS

**NanoSIMS Imaging of Micro- and Nanoscale Lipid Bilayer Phases.** Figure 2 shows a  $40 \times 40\ \mu\text{m}^2$  NanoSIMS image of a freeze-dried lipid bilayer formed by the deposition and annealing of a GUV composed of 2:2:1  $^2\text{H}$ -PSM/ $^{15}\text{N}$ -DOPC/ $^{13}\text{C}$ -cholesterol with 5 mol % 18-F- $\text{G}_{\text{M1}}$  onto an  $\text{SiO}_2/\text{Si}$  substrate, highlighting each of the four components based on the isotope or fluorine label, along with a secondary electron image. The secondary electron image immediately shows contrast between the lipid bilayer and the underlying oxidized silicon substrate. Furthermore, it shows contrast within the lipid

bilayer, indicating the presence of distinct phases with different electron densities. The molecule-specific images provide direct evidence for the colocalization of cholesterol and  $G_{MI}$  into micrometer-scale phases and PSM and DOPC into the interdomain region surrounding the  $G_{MI}$ /cholesterol-rich, micrometer-scale phases. Furthermore, the PSM image indicates formation of nanometer-scale phases within the  $G_{MI}$ /cholesterol-rich micrometer-scale phases. The composition of both the micrometer-scale phases and the interdomain region appears to contradict the general consensus that these phases are expected to be PSM/cholesterol-rich and DOPC-rich, respectively. However, the formation of nanometer-scale phases within the  $G_{MI}$ /cholesterol-rich micrometer-scale phases further supports the lipid raft hypothesis in both composition (i.e.,  $G_{MI}$ /PSM/cholesterol-rich compared to the surrounding phase) and length-scale. The sharp and fractal phase boundaries observed in the PSM image suggest a gel–liquid interface. However, the cholesterol image shows smooth and rounded phase boundaries that extend further into the interdomain region, suggesting a liquid–liquid interface. The  $G_{MI}$  image shows formation of nanometer scale phases within the interdomain region, while both the cholesterol and  $G_{MI}$  images suggest the accumulation of these components into nanometer scale phases at the lipid bilayer edge.

In order to perform compositional analysis of the phase separated lipid bilayer shown in Figure 2, phase boundaries were first defined using an ion intensity threshold value. Since the PSM image provided the best contrast between all the observed phases, the  $^{12}C^{2-}H^{-}$  ion image was used to classify three major compositionally distinct phases (Figure 3A): (1)

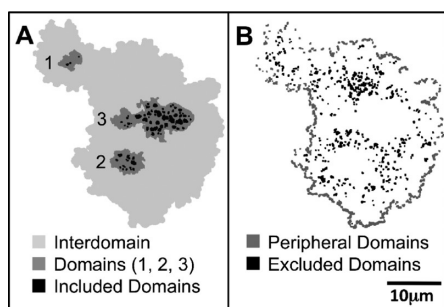


**Figure 3.** Maps of regions of interest within the lipid bilayer from Figure 2 highlighting the following: (A) three compositionally distinct phases corresponding to (1) interdomain region (light gray), (2) micrometer-scale domains 1, 2, and 3 (gray), and (3) nanometer-scale domains (black) localized within the micrometer-scale domains (referred to as “included” domains); (B) nanometer-scale domains localized within the interdomain region (black) and the edge of the lipid bilayer (referred to as “excluded” and “peripheral” domains, respectively).

the interdomain region (light gray); (2) the micrometer scale domains ( $d > 3 \mu m$ , gray), and (3) the nanometer scale domains ( $d \approx 100 \text{ nm}$  to  $1 \mu m$ , black) localized within the micrometer scale domains. Nanometer-scale domains were also observed in the interdomain region (Figure 3B, black) and at the edge of the lipid bilayers (Figure 3B, gray) and were resolved using the  $^{19}F^{-}$  ion,  $G_{MI}$ -specific image. Quantitative compositional analysis of these regions of interest was possible through the use of calibration curves from standard samples.

The overall composition ( $\pm$ uncertainty) of the lipid bilayer in Figure 3 (i.e., light gray, gray, and black regions in Figure 3A)

was determined by SIMS to be  $21.7 \pm 3.6 \text{ mol } \%$  cholesterol,  $56.2 \pm 4.6 \text{ mol } \%$  PSM,  $4.2 \pm 1.7 \text{ mol } \%$   $G_{MI}$ , and  $17.9 \pm 2.1 \text{ mol } \%$  DOPC (labeled “all” in Figure 4). The final composition

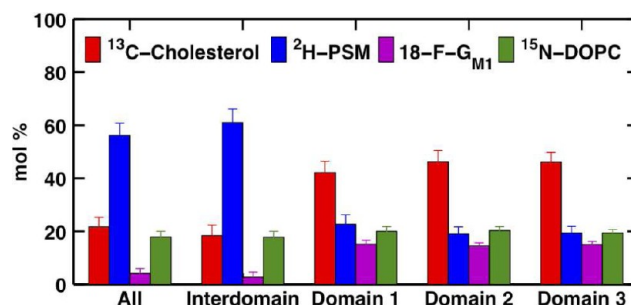


**Figure 4.** Quantitative compositional analysis of the entire lipid bilayer (all), the interdomain region (interdomain, light gray region in Figure 3A), and the three micrometer-scale domains (domains 1, 2, and 3 in order of increasing size, gray regions in Figure 3A).

determined from quantitative SIMS analysis was significantly different for PSM and DOPC and relatively similar for cholesterol and  $G_{MI}$  compared to the initial composition of the lipid mixture used to prepare the GUV (i.e., 19 mol % cholesterol, 38 mol % PSM, 5 mol %  $G_{MI}$ , and 38 mol % DOPC). Analysis of an additional 10 GUV lipid bilayers (see Table S6 and Figures S13–S22 in Supporting Information) suggests that the average composition ( $\pm 1 \text{ SD}$ ) of this GUV population is  $23.5 \pm 4.1 \text{ mol } \%$  cholesterol,  $45.4 \pm 12.4 \text{ mol } \%$  PSM,  $13.8 \pm 10.9 \text{ mol } \%$   $G_{MI}$ , and  $17.3 \pm 2.9 \text{ mol } \%$  DOPC (see Table S6 in Supporting Information), indicating significant GUV-to-GUV compositional variation. This further suggests that the lipid bilayers appear, on average, to be predominantly depleted in DOPC and would suggest a preferential adsorption of GUVs with a lowered DOPC content. However, preliminary work on simpler lipid mixtures suggests that cholesterol, and not DOPC, content is a major factor affecting the adsorption of GUVs while a small amount of PSM ( $>5 \text{ mol } \%$ ) can help improve the adsorption efficiency.<sup>46</sup> On the basis of ternary phase diagrams (without  $G_{MI}$ ), the compositional variation from GUV-to-GUV is such that two GUV populations, one in a two-phase regime and the other in a three-phase regime, would be expected. The discrepancy between the initial composition of the lipid mixture used to prepare the GUVs and the measured composition of the supported lipid bilayers by quantitative SIMS analysis might be the result of lipid demixing prior to GUV electroformation<sup>47</sup> (presumably as a result of GUV electroformation from a dry versus damp lipid film). Baykal-Caglar et al.<sup>47</sup> showed that the average cholesterol content in a multicomponent GUV population prepared using the method reported here had a standard deviation of 4 mol % in close agreement with our studies (4.1 mol %). The estimated compositional variation in their studies was based on imaging a GUV population by fluorescence microscopy and recording the temperature at which the phase behavior of each GUV changed from a phase separated state to a single-phase state and calculating the average temperature  $\pm 1 \text{ SD}$ . Furthermore, the calibration curves are based on chemically homogeneous mixtures, i.e., labeled molecule mixed with its unlabeled counterpart, and there may be effects from other chemically distinct components in a heterogeneous mixture. As a result, our quantitative compositional analysis is only an estimate of the actual composition. Furthermore, a control GUV lipid

bilayer sample also prepared with a 2:2:1  $^2\text{H}$ -sphingomyelin/ $^{15}\text{N}$ -DOPC/ $^{13}\text{C}$ -cholesterol but without 18-F- $\text{G}_{\text{M1}}$  revealed a final composition by quantitative SIMS analysis of  $29.6 \pm 3.8$  mol % cholesterol,  $57.5 \pm 3.5$  mol % PSM,  $0.8 \pm 1.9$  mol %  $\text{G}_{\text{M1}}$ , and  $12.1 \pm 2.2$  mol % DOPC. The final composition determined by SIMS analysis of the control sample is in close agreement with that of the sample with  $\text{G}_{\text{M1}}$  except for the very low  $\text{G}_{\text{M1}}$  content measurement falling just below the detection limit for 18-F- $\text{G}_{\text{M1}}$  (see Table S2 in Supporting Information).

The cholesterol-rich, micrometer-scale domains (labeled domains 1, 2, and 3 in order of increasing size in Figure 4 and colored gray in Figure 3) were surrounded by a cholesterol-poor, interdomain region (labeled interdomain in Figure 4 and colored light gray in Figure 3) with an averaged difference of 26 mol % between the two phases. Interestingly, these cholesterol-rich micrometer-scale domains correspond to PSM-poor regions while the surrounding interdomain corresponds to a PSM-rich region with an averaged difference of 40 mol % between the two phases. Furthermore, these micrometer-scale domains were also found to have an average of 12 mol % more  $\text{G}_{\text{M1}}$  than the interdomain region. Consequently, the micrometer-scale domains constitute a cholesterol-rich/PSM-poor/ $\text{G}_{\text{M1}}$ -rich phase whereas the interdomain region constitutes the opposite, i.e., a cholesterol-poor/PSM-rich/ $\text{G}_{\text{M1}}$ -poor phase. Even though DOPC does not appear to be homogeneously distributed throughout the lipid bilayer, the very low molar percent difference between the micrometer-scale domains and the interdomain region ( $\sim 2$  mol %) suggests that both phases have surprisingly similar DOPC content with the exception of few regional compositional inhomogeneities localized especially at the boundary of the micrometer-scale domains where DOPC appears to have been depleted.

As seen in Figure 2, a complex phase separation process occurred in which the micrometer-scale domains, the interdomain region, and the edge of the lipid bilayer displayed phase-separated, nanometer scale ( $d < 1 \mu\text{m}$ ) assemblies referred to as “included” ( $d = 379 \pm 229$  nm), “excluded” ( $d = 271 \pm 136$  nm), and “peripheral” ( $d = 435 \pm 203$  nm) domains, respectively (histograms in parts A, B, and C of Figure 5, respectively). Similar behavior was recently reported in a frequency modulated (FM)-AFM study showing that the diameter of domains in a DOPC/cholesterol/PSM-containing supported lipid bilayer is typically in the 500–3000 nm range.<sup>26</sup> The appearance of nanometer scale assemblies inside and outside the micrometer scale  $\text{L}_\alpha$  domains is also consistent with an AFM-imaging study<sup>48</sup> on the appearance of nanometer-scale domains within micrometer-scale domains and the interdomain region at the higher  $\text{G}_{\text{M1}}$  molar percent content also used here.

The excluded (Figure 3B, black) and peripheral (Figure 3B, gray) domains resolved here were identified using the  $^{19}\text{F}^-$  ion,  $\text{G}_{\text{M1}}$ -specific image. A total of 68, 318, and 125 nanodomains were resolved within the micrometer-scale domains, the interdomain region, and the edge of the lipid bilayer, respectively. The nanometer-scale domains localized at the periphery of the lipid bilayer were often highly interconnected making it difficult to resolve individual domains using a single criterion. As a result, the agglomeration of nanometer scale phases into larger assemblies accounts for the larger sizes observed in the size distribution histogram. Quantitative compositional analysis (Figure 6) suggests that (1) the included nanodomains have similar cholesterol, more PSM, and less  $\text{G}_{\text{M1}}$  and DOPC content than the micrometer-scale domains, (2) the excluded nanodomains have similar cholesterol and DOPC

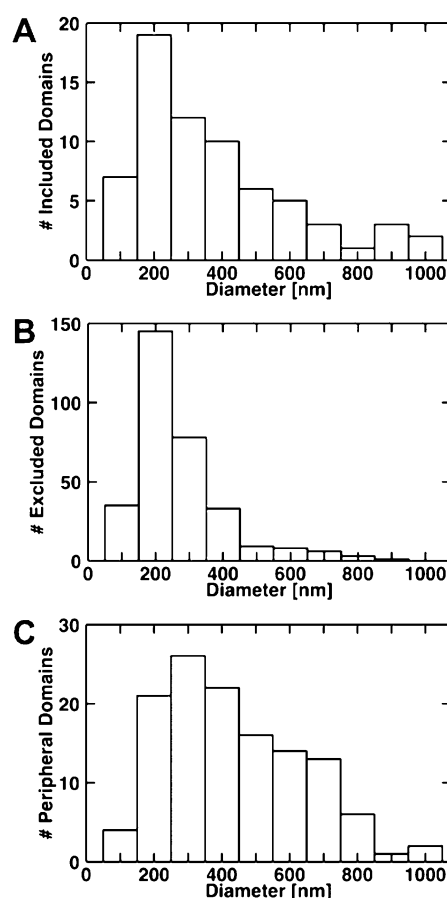


**Figure 5.** Size distributions of the nanometer-scale domains localized within the micrometer-scale domains, the interdomain region, and the edge of the lipid bilayer referred to as included (A), excluded (B), and peripheral domains (C), respectively.

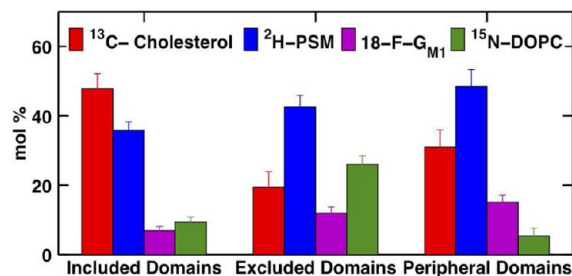


**Figure 6.** Quantitative compositional analysis of the nanometer-scale domains localized within the micrometer-scale domains, the interdomain region, and the edge of the lipid bilayer referred to as included, excluded, and peripheral domains, respectively.

content, less PSM, and more  $\text{G}_{\text{M1}}$  than the interdomain region, and (3) the peripheral domains have more cholesterol and  $\text{G}_{\text{M1}}$  and less PSM and DOPC than the interdomain region. Because peripheral domain formation is dictated not only by phase separation processes (which include the effect of the support) but also by lipid bilayer edge effects, they are omitted from further discussion on phase separation processes. Consequently, the included nanodomains are referred to as PSM-rich in relation to the micrometer scale domains whereas the excluded nanodomains are referred to as  $\text{G}_{\text{M1}}$ -rich in relation to the interdomain region.



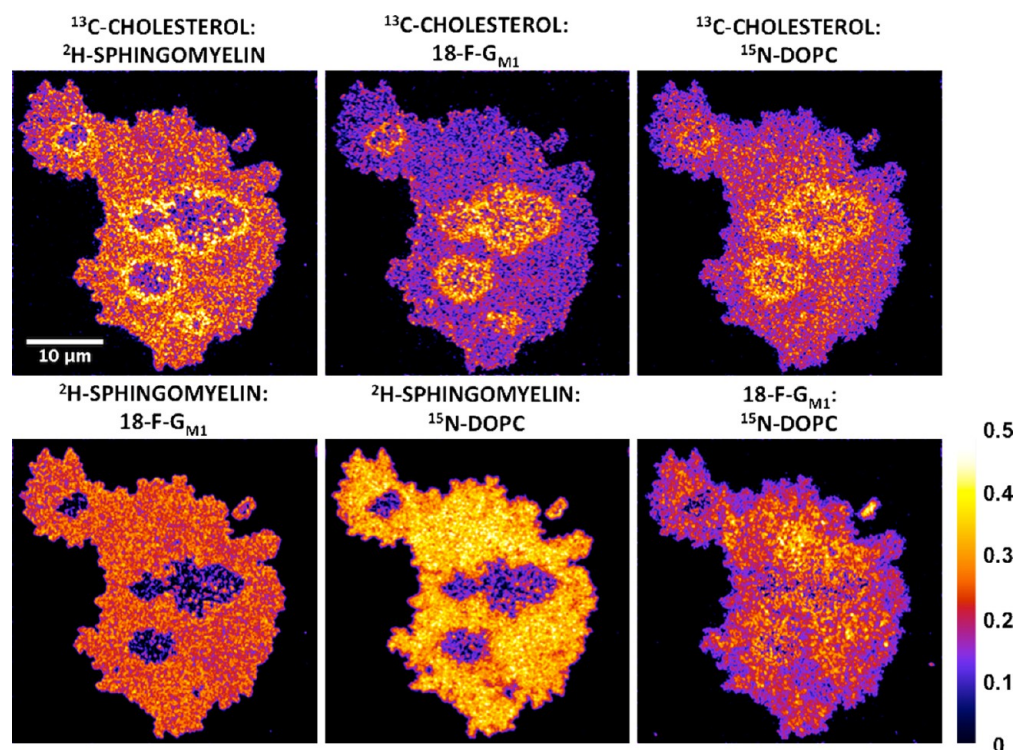


**Figure 7.** Colocalization of lipid bilayer components. The color bar represents colocalization score values. Score values less than 0.3 indicate low colocalization, and score values more than 0.3 indicate high colocalization (see text).

**Colocalization of Membrane Components.** Figure 7 shows the colocalization image for pairs of membrane components in the lipid bilayer depicted in Figure 2. Colocalization images are generated by calculating the square root of the product between the normalized, molecule-specific images given by

$$S_{1,2} = \left[ \frac{x_1 - x_{1,\min}}{x_{1,\max} - x_{1,\min}} \times \frac{x_2 - x_{1,\min}}{x_{2,\max} - x_{2,\min}} \right]^{1/2}$$

where  $S_{1,2}$ ,  $x$ ,  $x_{\max}$ , and  $x_{\min}$  represent score value between membrane components 1 and 2, pixel value, maximum pixel value, and minimum pixel value, respectively. Normalization of the molecule-specific images allowed comparison between all binary images using a single score scale. Score values above 0.3 indicate high colocalization, while score values below 0.3 indicate low colocalization.

Figure 7 indicates high colocalization of cholesterol and sphingomyelin at the boundary of micrometer-scale phases (domains 1, 2, and 3) extending approximately 1.5  $\mu\text{m}$  into the interdomain region (referred to as “domain boundary region”). Cholesterol and sphingomyelin also colocalize within the nanometer scale phases localized within these micrometer-scale domains (included domains) and the nanometer scale phases at the periphery of the lipid bilayer (peripheral domains). Furthermore, Figure 7 indicates high colocalization of cholesterol and ganglioside  $\text{G}_{\text{M1}}$  within domains 1, 2, and 3 and the domain boundary region, and the nanometer-scale phases at the periphery of the lipid bilayer (peripheral domains). It also indicates high colocalization of cholesterol and DOPC at the domain boundary region. Figure 7 also indicates high colocalization of sphingomyelin and ganglioside  $\text{G}_{\text{M1}}$  within the interdomain region, the included, excluded, and peripheral domains. It also indicates high colocalization of

sphingomyelin and DOPC within the interdomain region and the nanometer scale phases within the interdomain region (i.e., excluded domains). Lastly, Figure 7 indicates high colocalization between ganglioside  $\text{G}_{\text{M1}}$  and DOPC within the excluded domains.

## DISCUSSION

**Monofluorinated 18-F- $\text{G}_{\text{M1}}$  Mimics Native  $\text{G}_{\text{M1}}$  in Live Cell and Model Membranes.** Fluorine substitution is a useful strategy for providing contrast in NanoSIMS imaging, since it is easily resolved from isobaric interferences (i.e.,  $^{18}\text{O}^1\text{H}^-$  at mass 19); the high electron affinity of fluorine leads to particularly high sensitivity, and it affords minimal background. However, it is important to confirm that fluorine substitution does not affect the biological and physical properties of the labeled molecule.

Fluorine substitution for hydrogen atoms has been widely used to modify biologically active molecules in bioorganic and medicinal chemistry.<sup>49–58</sup> Monofluorination on the hydrocarbon chain of lipids has been proven to exhibit minimal effect on its biophysical properties.<sup>59</sup> We designed and synthesized single fluorine labeled gangliosides for the detection of assemblies in which such molecules participate. Fluorine and hydrogen are isoteric; therefore, we expect that substitution with a single fluorine atom at position 18 should not significantly alter the physical properties of the molecule.<sup>60</sup> Nonetheless, we evaluated the biological behavior of 18-F- $\text{G}_{\text{M1}}$  compared to native  $\text{G}_{\text{M1}}$ . The ability of 18-F- $\text{G}_{\text{M1}}$  to trigger  $\text{Ca}^{2+}$  influx was interrogated in Jurkat cells and found to be similar to that induced by native  $\text{G}_{\text{M1}}$  (see Figure S2 in Supporting Information). Furthermore, the incorporation of 18-F- $\text{G}_{\text{M1}}$  into mammalian cell surfaces and recognition by cholera toxin B subunit (CTB) was confirmed by flow cytometry (see Figure S3 in Supporting Information). The

incorporation levels of 18-F- $G_{M1}$  into CHO-K1 cells were found to be similar to native  $G_{M1}$ . In addition, the biophysical properties and phase behavior of 18-F- $G_{M1}$  were analyzed by AFM in phase separated SLBs and shown to mirror native  $G_{M1}$  (see Figure S4 in Supporting Information).

On the other hand, there have been studies on multilamellar vesicles composed of monofluorinated DPPC (F-DPPC, with a single F atom at position 16 of the palmitic acid chain) mixed with native DPPC that have shown the appearance of an interdigitated monolayer phase, presumably as the result of strong interactions between the headgroup of a lipid and the highly polar fluorine atom at the methyl terminus of the *sn*-2 chain of another lipid, to be concentration dependent. This effect becomes more apparent at concentrations higher than 30 mol % F-DPPC,<sup>61</sup> and addition of cholesterol has been shown to inhibit formation of this interdigitated monolayer phase.<sup>62</sup> On the basis of these studies, we do not expect the formation of an interdigitated phase in our system, since only 5 mol % of a monofluorinated  $G_{M1}$  and as much as 19 mol % cholesterol were incorporated into the GUVs. In addition, AFM imaging results (see Figure S4 in Supporting Information) showed no evidence of an interdigitated monolayer phase, as determined from membrane thickness measurements showing height values that span an entire lipid bilayer as opposed to half a lipid bilayer characteristic of an interdigitated monolayer phase.<sup>63</sup> Taken together, there is no evidence of an interdigitated monolayer phase in our system. Therefore, we conclude that substitution of a single hydrogen atom with fluorine at position 18 on the stearic acid chain of  $G_{M1}$  does not significantly disturb the physical behavior of the molecule within lipid membranes when incorporated at low molar percentages.

Furthermore, our SIMS imaging results indicate that  $G_{M1}$  assembly into micrometer scale phases is strongly cholesterol dependent. On the other hand,  $G_{M1}$  assembly into nanometer scale phases is likely dictated by interactions between the oligosaccharide headgroups. The latter assessment is based on Langmuir monolayer studies that showed the condensing effect of the oligosaccharide headgroup in  $G_{M1}$ -containing monolayers and further showed, in contrast, that 18:0 ceramide (essentially  $G_{M1}$  without its headgroup) or 18:0 ceramide EO<sub>16</sub> (with the polyethylene chain modeling the bulky oligosaccharide headgroup in  $G_{M1}$ ) containing monolayers do not induce condensation.<sup>64</sup>

In sum, the AFM, FACS, and  $Ca^{2+}$  signaling assay data show that a terminally monofluorinated  $G_{M1}$ , 18-F- $G_{M1}$ , has similar biophysical and biological properties as native  $G_{M1}$  and serves as a nonperturbing proxy for the native ganglioside  $G_{M1}$  that is ideally suited for NanoSIMS experiments. Interestingly, when a  $G_{M1}$  analogue with fluorine substitution in the middle of the stearic acid chain at position 12 was used to form SLBs, separation between gel and  $L_d$  phases was different (see Figure S25 in Supporting Information). This is presumably the result of a change in tilt angle leading 12-F- $G_{M1}$  to behave differently in model membranes.<sup>59</sup>

**$G_{M1}$  and Cholesterol Colocalize within Liquid Ordered Micrometer-Scale Phases.** The molecule-specific images obtained from NanoSIMS analysis of a phase separated lipid bilayer presented in Figures 2 and 3 illustrate the presence of complex phases at the micro- and nanometer scales. The micrometer scale phase behavior of our system was first characterized, prior to SIMS imaging, by fluorescence microscopy using a small amount of a fluorescent lipid (0.05 mol % TR-DHPE) that preferentially partitions into disordered

phases. Fluorescence microscopy images (see Figure S5 in Supporting Information) revealed the formation of micrometer scale  $L_o$  domains with low fluorescence intensity (FI) values surrounded by an  $L_d$  interdomain region with high FI values. Often a differential partitioning of the fluorophore in the region spanning a few micrometers from the edge into the lipid bilayer was also observed with medium FI values; this was attributed to edge effects, an inevitable consequence of the sample preparation, and these edges were avoided in discussions of phase separation processes. The observation of micrometer scale phase coexistence reported here is consistent with phase diagrams developed from fluorescence microscopy imaging of a canonical lipid raft mixture at room temperature that places a 2:2:1 PSM/DOPC/cholesterol-containing GUV in a two-phase regime corresponding to  $L_o$  domains, presumably sphingomyelin and cholesterol-rich, surrounded by an  $L_d$  interdomain region, presumably phosphatidylcholine-rich and cholesterol poor.<sup>65–67</sup> Furthermore, AFM imaging on the incorporation of the ganglioside  $G_{M1}$  into the canonical lipid raft mixture at low molar percentages (<5 mol %) suggested the preferential partitioning of  $G_{M1}$  into these  $L_o$  domains that are presumably sphingomyelin and cholesterol-rich.<sup>48</sup> The SIMS images presented here provide, for the first time, direct evidence for the colocalization of  $G_{M1}$  and cholesterol and show that  $G_{M1}$  partitions instead into  $L_o$ , cholesterol-rich/PSM-poor domains surrounded by an  $L_d$ , PSM-rich interdomain region.

**Formation of Nanometer Scale Phases: Comparisons with Other Data.**  $G_{M1}$  has been used as a raft marker in many studies, where it is visualized by using a derivative that has a fluorophore on one of the fatty acid chains,<sup>68</sup> by binding a fluorescently labeled CTB subunit,<sup>69,70</sup> or by AFM, exploiting the subtle height difference associated with the oligosaccharide headgroup.<sup>48,71</sup> Each method introduces a different set of issues, and unfortunately, precisely the same set of lipid mixtures and conditions are rarely used, making comparisons difficult. Furthermore, the direct, quantitative analysis of complex phases is not possible without molecule-specific information of the sort provided by imaging mass spectrometry. In the following discussion we draw on this and other literature to the extent possible to help interpret our data.

The appearance of three distinct phases within the lipid bilayer shown in Figure 3 is consistent with previous studies on fluorescence intensity, anisotropy, and lifetimes of trans-parinaric acid (tPA) containing giant multilamellar vesicles (GPMVs) at room temperature that places this same mixture (i.e., 2:2:1 PSM/DOPC/cholesterol) in a three-phase regime corresponding to  $L_d$ ,  $L_o$ , and gel phases.<sup>72</sup> However, the SIMS studies provide unique quantitative compositional analysis of these phases that could only be inferred indirectly in earlier measurements. Yuan et al. (2002) imaged the distribution of  $G_{M1}$  (at 1 and 5 mol %) in a 1:1:1 DOPC/sphingomyelin/cholesterol-containing lipid monolayer on mica using AFM<sup>47</sup> and showed the formation of small (40–100 nm)  $G_{M1}$ -rich domains localized within the more ordered, micrometer scale, presumably PSM/cholesterol-rich domain phase at the lower  $G_{M1}$  content and also within the surrounding, less-ordered, DOPC-rich interdomain phase at the higher  $G_{M1}$  content. Their observations<sup>48</sup> of height differences between nanometer-scale phases and the surrounding region using AFM are qualitatively consistent with our observations of compositional variations using NanoSIMS data. At the higher  $G_{M1}$  content, both methods revealed three main regions corresponding to (1) a more ordered, micrometer-scale domain phase, (2) a



surrounding, less ordered, interdomain phase, and (3) nanometer scale phases localized within phases 1 and 2. However, qualitative and quantitative SIMS analysis presented in Figures 4 and 5 on the composition of these phases revealed that PSM-rich, nanometer-scale domains preferred to partition within the more ordered, cholesterol-rich/PSM-poor/ $G_{M1}$ -rich phase, while  $G_{M1}$ -rich, nanometer-scale domains preferred to partition within the surrounding, disordered, cholesterol-poor/PSM-rich/ $G_{M1}$ -poor interdomain phase. Since phase behavior is dictated by composition, temperature, and pressure on a surface (i.e., including substrate and lipid bilayer edge effects), differences in these parameters may account for the observed differences between their system and ours.

Compositional analysis of the  $G_{M1}$ -specific image suggests that  $G_{M1}$  prefers partitioning into both micro- and nanometer scale ordered phases that are surrounded by a disordered phase. The observation of  $G_{M1}$  partitioning into micrometer scale ordered phases is consistent with previous studies. However, there is little and often contradicting evidence supporting its localization within a distributed, nanometer scale phase. A fluorescence microscopy and fluorescence correlation spectroscopy (FCS) study using DiIC<sub>18</sub> and CTB-Alexa488 as probes<sup>69</sup> showed the preferential partitioning of  $G_{M1}$  into  $L_o$  micrometer scale domains and no indication of an additional, subresolution microdomain structure within these visible domains. In contrast, fluorescence microscopy imaging of native membranes showed no visible micrometer-scale phase separation and yet FCS analysis showed anomalous diffusion supporting a subresolution structure of small phases dispersed in a continuous phase and limited mobility suggesting its restriction to nanometer scale assemblies that are associated with the cytoskeleton.<sup>69</sup> Furthermore, a fluorescence microscopy study<sup>70</sup> using DiIC<sub>12</sub> and CTB-Alexa488 as probes suggested that CTB binding to the membranes, and not the coalescence of pre-existing nanoscale structures, is responsible for creating new phases. On the other hand, an AFM study<sup>71</sup> provided convincing evidence for the presence of pre-existing  $G_{M1}$ -rich nanoscale (10–60 nm in size) structures at  $G_{M1}$  concentrations above 0.5 mol % in POPC lipid bilayers. The direct SIMS imaging of the lateral distribution of  $G_{M1}$  within a model membrane composed of a lipid raft mixture suggests that  $G_{M1}$  associates with cholesterol-dependent, micrometer-scale ordered phases as well as cholesterol-independent, nanometer scale ordered phases, both dispersed in a liquid disordered, PSM-rich interregion.

The appearance of nanometer scale assemblies and their agglomeration into micrometer scale clusters within the phase separated lipid bilayer presented in Figure 2 is consistent with a recent NanoSIMS imaging study on the cholesterol-dependent phase separation of a ternary lipid bilayer mixture composed of 1:1 <sup>15</sup>N-DLPC/<sup>2</sup>H-DSPC with various amounts of cholesterol ranging from 0 to 19 mol %, where cholesterol was not imaged, suggesting the agglomeration of gel-phase, DSPC-rich nanoscopic domains into micrometer-scale clusters at the highest cholesterol content.<sup>73</sup> Domain sizes are dictated by the thermal history of the sample.<sup>74</sup> In the system presented in this paper, heated ( $T > 70$  °C) GUVs were fused to SiO<sub>2</sub>/Si substrates at room temperature and incubated for 30 min followed by incubation at 70 °C for 30 min and cooled to room temperature at a rate of 5 °C/h. This slow cooling treatment is meant to minimize the formation of kinetically trapped regions and allows instead for a phase separation process that is closer to equilibrium.

## CONCLUSION

The direct observation of lipid rafts in mammalian cell membranes has been of interest since they were first described<sup>75</sup> and assigned important biological roles.<sup>76</sup> We have developed a direct method to visualize the spatial organization and preferential partitioning of a monofluorinated derivative of  $G_{M1}$  with cholesterol by NanoSIMS in a canonical lipid raft mixture. As judged by functional and biophysical assays, 18-F- $G_{M1}$  recapitulates the properties of native  $G_{M1}$  and serves as a minimally perturbed proxy. 18-F- $G_{M1}$  was examined in the context of a quaternary mixture of lipids in SLBs by NanoSIMS. Quantitative image analysis demonstrates preferential colocalization of  $G_{M1}$  with cholesterol in lipid bilayers, without the need for staining or modification with labels. Furthermore, the SIMS imaging also affords detailed information for all components, such as the colocalization of PSM and DOPC within the interdomain region, which has not been reported using AFM and other techniques. Although the lateral resolution of NanoSIMS is modest compared to AFM, it reveals molecule specific information of the lateral organization. These studies set the stage for comparing the behavior of a wide variety of previously postulated membrane assemblies including lipid rafts in cellular membranes. Studies along these lines are underway in our laboratories.

## ASSOCIATED CONTENT

### Supporting Information

Biosynthesis of <sup>13</sup>C-cholesterol isotopomers (Figure S1); synthesis of <sup>15</sup>N-DOPC; synthesis of monofluorinated  $G_{M1}$  (Scheme S1); calcium signaling assay (Figure S2); FACS (Figure S3); AFM (Figure S4); fluorescence microscopy imaging (Figure S4); SIMS high mass resolving spectra (Figure S5); calibration curves from standard samples for quantitative SIMS analysis (Figure S6 and Tables S1 and S2); quantitative and error analysis of regions of interest in Figure 2 (Figures S7–S12 and Table S3–S5); SIMS imaging and quantitative analysis of additional GUV lipid bilayers (Tables S6–S7 and Figure S13–S24); NanoSIMS images of a lipid bilayer composed of another monofluorinated  $G_{M1}$  (12-F- $G_{M1}$ ) analogue (Figure S25). This material is available free of charge via the Internet at <http://pubs.acs.org>.

## AUTHOR INFORMATION

### Corresponding Author

mmlozano@gmail.com; krishna.kumar@tufts.edu; sboxer@stanford.edu

### Notes

The authors declare no competing financial interest.

## ACKNOWLEDGMENTS

M.M.L. and S.G.B. are particularly grateful to Dr. Peter Weber at the Lawrence Livermore National Laboratory, CA, for initial training on the NanoSIMS 50 at Livermore. M.M.L. and S.G.B. thank the Khosla Lab at Stanford University, CA, for access to their cell culturing facilities; the Stanford University Mass Spectrometry facilities for help with the analysis of <sup>13</sup>C labeled cholesterol isotopomers; Charles Hitzman at the Stanford Nanocharacterization Laboratory for instrument support on the NanoSIMS 50L. This work was supported in part by the National Institutes of Health (Grant GM069630 to S.G.B. and Grants GM65500 and CA125033 to K.K.), and the National Science Foundation Biophysics Program (S.G.B.). M.M.L. was

supported by a Ruth L. Kirschstein NRSA Postdoctoral Fellowship. The Cameca NanoSIMS 50L at the Stanford Nano Shared Facilities is supported by the National Science Foundation (Grant 0922648). The ESI-MS and NMR facilities at Tufts, MA, are supported by the National Science Foundation (Grants 0320783 and 0821508).

## REFERENCES

- (1) Lingwood, D.; Simons, K. *Science* **2010**, 327, 46–50.
- (2) Hancock, J. F. *Nat. Rev. Mol. Cell Biol.* **2006**, 7, 456–462.
- (3) Feigenson, G. W. *Biochim. Biophys. Acta* **2009**, 1788, 47–52.
- (4) Dietrich, C.; Yang, B.; Fujiwara, T.; Kusumi, A.; Jacobson, K. *Biophys. J.* **2002**, 82, 274–284.
- (5) Schütz, G. J.; Kada, G.; Pastushenko, V. P.; Schindler, H. *EMBO J.* **2000**, 19, 892–901.
- (6) Pralle, A.; Keller, P.; Florin, E. L.; Simons, K.; Hörber, J. K. *J. Cell Biol.* **2000**, 148, 997–1008.
- (7) Varma, R.; Mayor, S. *Nature* **1998**, 394, 798–801.
- (8) Heberle, F. A.; Wu, J.; Goh, S. L.; Petruziolo, R. S.; Feigenson, G. W. *Biophys. J.* **2010**, 99, 3309–3318.
- (9) Bader, A. N.; Hoetzel, S.; Hofman, E. G.; Voortman, J.; van Bergen en Henegouwen, P. M. P.; van Meer, G.; Gerritsen, H. C. *ChemPhysChem* **2011**, 12, 475–483.
- (10) Sezgin, E.; Schwille, P. *Cold Spring Harbor Perspect. Biol.* **2011**, 3, 9803.
- (11) Sharonov, A.; Hochstrasser, R. M. *Proc. Natl. Acad. Sci. U.S.A.* **2006**, 103, 18911–18916.
- (12) Giannone, G.; Hosy, E.; Levet, F.; Constals, A.; Schulze, K.; Sobolevsky, A. I.; Rosconi, M. P.; Gouaux, E.; Tampé, R.; Choquet, D.; Cognet, L. *Biophys. J.* **2010**, 99, 1303–1310.
- (13) Sun, Y.; Wallrabe, H.; Booker, C. F.; Day, R. N.; Periasamy, A. *Biophys. J.* **2010**, 99, 1274–1283.
- (14) Betzig, E.; Patterson, G. H.; Sougrat, R.; Lindwasser, O. W.; Olenych, S.; Bonifacino, J. S.; Davidson, M. W.; Lippincott-Schwartz, J.; Hess, H. F. *Science* **2006**, 313, 1642–1645.
- (15) Hess, S. T.; Girirajan, T. P. K.; Mason, M. D. *Biophys. J.* **2006**, 91, 4258–4272.
- (16) Rust, M. J.; Bates, M.; Zhuang, X. *Nat. Methods* **2006**, 3, 793–795.
- (17) Eggeling, C.; Ringemann, C.; Medda, R.; Schwarzmann, G.; Sandhoff, K.; Polyakova, S.; Belov, V. N.; Hein, B.; Middendorff, von, C.; Schönle, A.; Hell, S. W. *Nature* **2009**, 457, 1159–1162.
- (18) Sahl, S. J.; Leutenegger, M.; Hilbert, M.; Hell, S. W.; Eggeling, C. *Proc. Natl. Acad. Sci. U.S.A.* **2010**, 107, 6829–6834.
- (19) Mueller, V.; Ringemann, C.; Honigsmann, A.; Schwarzmann, G.; Medda, R.; Leutenegger, M.; Polyakova, S.; Belov, V. N.; Hell, S. W.; Eggeling, C. *Biophys. J.* **2011**, 101, 1651–1660.
- (20) van den Bogaart, G.; Meyenberg, K.; Risselada, H. J.; Amin, H.; Willig, K. I.; Hubrich, B. E.; Dier, M.; Hell, S. W.; Grubmüller, H.; Diederichsen, U.; Jahn, R. *Nature* **2011**, 479, 552–555.
- (21) Ge, M.; Field, K. A.; Aneja, R.; Holowka, D.; Baird, B.; Freed, J. H. *Biophys. J.* **1999**, 77, 925–933.
- (22) Giocondi, M. C.; Vié, V.; Lesniewska, E.; Goudonnet, J. P.; Le Grimellec, C. *J. Struct. Biol.* **2000**, 131, 38–43.
- (23) Fukuma, T.; Jarvis, S. *Rev. Sci. Instrum.* **2006**, 77, 043701.
- (24) Fukuma, T.; Higgins, M. J.; Jarvis, S. P. *Biophys. J.* **2007**, 92, 3603–3609.
- (25) Loh, S.-H.; Jarvis, S. P. *Langmuir* **2010**, 26, 9176–9178.
- (26) Sheikh, K. H.; Jarvis, S. P. *J. Am. Chem. Soc.* **2011**, 133, 18296–18303.
- (27) Sheikh, K. H.; Giordani, C.; Kilpatrick, J. I.; Jarvis, S. P. *Langmuir* **2011**, 27, 3749–3753.
- (28) Yu, J. J.; Fischman, D. A.; Steck, T. L. *J. Supramol. Struct.* **1973**, 1, 233–248.
- (29) Prinz, C.; Höök, F.; Malm, J.; Sjövall, P. *Langmuir* **2007**, 23, 8035–8041.
- (30) Popov, J.; Vobornik, D.; Coban, O.; Keating, E.; Miller, D.; Francis, J.; Petersen, N. O.; Johnston, L. J. *Langmuir* **2008**, 24, 13502–13508.
- (31) Benabdellah, F.; Seyer, A.; Quinton, L.; Touboul, D.; Brunelle, A.; Laprèvote, O. *Anal. Bioanal. Chem.* **2010**, 396, 151–162.
- (32) Saleem, M.; Galla, H.-J. *Biochim. Biophys. Acta* **2010**, 1798, 730–740.
- (33) Yang, Y.-L.; Xu, Y.; Straight, P.; Dorrestein, P. C. *Nat. Chem. Biol.* **2009**, 5, 885–887.
- (34) Snel, M. F.; Fuller, M. *Anal. Chem.* **2010**, 82, 3664–3670.
- (35) Lechene, C.; Hillion, F.; McMahon, G.; Benson, D.; Kleinfeld, A. M.; Kampf, J. P.; Distel, D.; Luyten, Y.; Bonventre, J.; Hentschel, D.; Park, K. M.; Ito, S.; Schwartz, M.; Benichou, G.; Slodzian, G. *J. Biol.* **2006**, 5, 20.
- (36) Galli Marxer, C.; Kraft, M. L.; Weber, P. K.; Hutcheon, I. D.; Boxer, S. G. *Biophys. J.* **2005**, 88, 2965–2975.
- (37) Kraft, M. L.; Fishel, S. F.; Marxer, C. G.; Weber, P. K.; Hutcheon, I. D.; Boxer, S. G. *Appl. Surf. Sci.* **2006**, 252, 6950–6956.
- (38) Kraft, M. L.; Weber, P. K.; Longo, M. L.; Hutcheon, I. D.; Boxer, S. G. *Science* **2006**, 313, 1948–1951.
- (39) Boxer, S. G.; Kraft, M. L.; Weber, P. K. *Annu. Rev. Biophys.* **2009**, 38, 53–74.
- (40) Liu, Z.; Kumar, K. *Synthesis* **2010**, 2010, 1905–1908.
- (41) Shivapurkar, R.; Souza, C. M.; Jeannerat, D.; Riezman, H. *J. Lipid Res* **2011**, 52, 1062–1065.
- (42) Kelleher, J. K.; Kharroubi, A. T.; Aldaghlis, T. A.; Shambat, I. B.; Kennedy, K. A.; Holleran, A. L.; Masterson, T. M. *Am. J. Physiol.* **1994**, 266, E384–E395.
- (43) Cholesterol label alternatives suitable for SIMS imaging included  $^2\text{H}$ ,  $^{18}\text{O}$ , and  $^{19}\text{F}$ . However, each presented issues that led us to pursue  $^{13}\text{C}$  as the label of choice.  $^2\text{H}_7$ -Cholesterol is commercially available but conflicts with other deuterated molecules of interest (i.e.,  $^2\text{H}_{31}$ -PSM in these studies).  $^{18}\text{O}$ -Cholesterol was synthesized and tested, but signal-to-noise was poor even after  $^{18}\text{O}$ -depletion of the  $\text{SiO}_2/\text{Si}$  substrates (Mary Kraft and S.G.B., unpublished results).  $^{19}\text{F}$ -Cholesterol is commercially available, but it conflicts with other fluorinated molecules of interest (i.e.,  $^{19}\text{F}$ -GM1 in these studies) and its biophysical properties were drastically different from those of native cholesterol at the high molar concentrations used in these studies.
- (44) Schwarzmann, G.; Sandhoff, K. *Methods Enzymol.* **1987**, 138 (26), 319–341.
- (45) Angelova, M. I.; Soleau, S.; Meleard, P.; Faucon, J.-F.; Bothorel, P. *Springer Proc. Phys.* **1992**, 66, 178–182.
- (46) Our data (Monica Lozano and S.G.B., not published) suggests that GUVs (prepared under the same conditions as those described here) composed of 90–95 mol %  $^{15}\text{N}$ -DOPC and 5–10 mol % 18-F-GM1 adsorb to the substrates just as effectively as those described in this paper. So it is unlikely that DOPC alone is responsible for the apparent lowered adsorption efficiency. Preliminary results also indicate that the addition of  $^{13}\text{C}$ -cholesterol (10, 20, and 30 mol %) to a  $^{15}\text{N}$ -DOPC/5 mol % 18-F-GM1 lipid mixture prevents GUVs from adsorbing to the substrates. However, in another control, the addition of a small amount of 2H-PSM (8 mol % 2H-PSM, 16 mol %  $^{13}\text{C}$ -cholesterol, 5 mol % 18-F-GM1, and 71 mol %  $^{15}\text{N}$ -DOPC vs 16 mol %  $^{13}\text{C}$ -cholesterol, 5 mol % 18-F-GM1, and 79 mol %  $^{15}\text{N}$ -DOPC) induces the adsorption of GUVs but in a less effective manner as those compositions described in this paper.
- (47) Baykal-Caglar, E.; Hassan-Zadeh, E.; Saremi, B.; Huang, J. *Biochim. Biophys. Acta* **2012**, 1818 (11), 2598–2604.
- (48) Yuan, C.; Furlong, J.; Burgos, P.; Johnston, L. *Biophys. J.* **2002**, 82, 2526–2535.
- (49) Muller, K.; Faeh, C.; Diederich, F. *Science* **2007**, 317, 1881–1886.
- (50) Berger, R.; et al. *Chem. Soc. Rev.* **2011**, 40, 3496–3508.
- (51) Yoder, N. C.; Kumar, K. *Chem. Soc. Rev.* **2002**, 31, 335–341.
- (52) Meng, H.; Krishnaji, S. T.; Beinborn, M.; Kumar, K. *J. Med. Chem.* **2008**, 51 (22), 7303–7307.

- (53) Meng, H.; Kumar, K. *J. Am. Chem. Soc.* **2007**, *129*, 15615–15622.
- (54) Tang, Y.; Ghirlanda, G.; Petka, W. A.; Nakajima, T.; DeGrado, W. F.; Tirrell, D. A. *Angew. Chem., Int. Ed.* **2001**, *40*, 1494–1496.
- (55) Tang, Y.; Ghirlanda, G.; Vaidehi, N.; Kua, J.; Mainz, D. T.; Goddard, W. A.; DeGrado, W. F.; Tirrell, D. A. *Biochemistry* **2001**, *40*, 2790–2796.
- (56) Niemz, A.; Tirrell, D. A. *J. Am. Chem. Soc.* **2001**, *123*, 7407–7413.
- (57) Naarmann, N.; Bilgicer, B.; Meng, H.; Kumar, K.; Steinem, C. *Angew. Chem., Int. Ed.* **2006**, *45*, 2588–2591.
- (58) Bilgicer, B.; Kumar, K. *Proc. Natl. Acad. Sci. U.S.A.* **2004**, *101*, 15324–15329.
- (59) O'Hagan, D. *Chem. Commun.* **1997**, *7*, 645–652.
- (60) Dunitz, J. D. *ChemBioChem* **2004**, *5*, 614–621.
- (61) Smith, E. A.; van Gorkum, C. M.; Dea, P. K. *Biophys. Chem.* **2010**, *147*, 20–27.
- (62) Smith, E. A.; Wang, W.; Dea, P. K. *Chem. Phys. Lipids* **2012**, *165*, 151–159.
- (63) Sanii, B.; Szmodis, A. W.; Bricarello, D. A.; Oliver, A. E.; Parikh, A. N. *J. Phys. Chem. B* **2010**, *114*, 215–219.
- (64) Frey, S. L.; Chi, E. Y.; Arratia, C.; Majewski, J.; Kjaer, K.; Lee, K. Y. C. *Biophys. J.* **2008**, *94*, 3047–3064.
- (65) Koenig, B.; Kruger, S.; Orts, W.; Majkrzak, C.; Berk, N.; Silverton, J.; Gawrisch, K. *Langmuir* **1996**, *12*, 1343–1350.
- (66) Veatch, S. L.; Keller, S. L. *Phys. Rev. Lett.* **2005**, *94*, 148101.
- (67) Marsh, D. *Biochim. Biophys. Acta* **2009**, *1788*, 2114–2123.
- (68) Nakagawa, T.; Tani, M.; Kita, K.; Ito, M. *J. Biochem.* **1999**, *126*, 604–611.
- (69) Bacia, K.; Scherfeld, D.; Kahya, N.; Schwille, P. *Biophys. J.* **2004**, *87*, 1034–1043.
- (70) Hammond, A. T.; Heberle, F. A.; Baumgart, T.; Holowka, D.; Baird, B.; Feigenson, G. W. *Proc. Natl. Acad. Sci. U.S.A.* **2005**, *102*, 6320–6325.
- (71) Shi, J.; Yang, T.; Kataoka, S.; Zhang, Y.; Diaz, A. J.; Cremer, P. S. *J. Am. Chem. Soc.* **2007**, *129*, 5954–5961.
- (72) Nyholm, T. K. M.; Lindroos, D.; Westerlund, B.; Slotte, J. P. *Langmuir* **2011**, *27*, 8339–8350.
- (73) Anderton, C. R.; Lou, K.; Weber, P. K.; Hutcheon, I. D.; Kraft, M. L. *Biochim. Biophys. Acta* **2011**, *1808*, 307–315.
- (74) Goksu, E. I.; Vanegas, J. M.; Blanchette, C. D.; Lin, W.-C.; Longo, M. L. *Biochim. Biophys. Acta* **2009**, *1788*, 254–266.
- (75) Simons, K.; Van Meer, G. *Biochemistry* **1988**, *387*, 6197–6202.
- (76) Simons, K. K.; Ikonen, E. E. *Nature* **1997**, *387*, 569–572.